ATLAS NOTE

ATLAS-CONF-2015-021

27th June 2015

Measurement of correlations between dijet-asymmetry and event-shape variables in Pb+Pb collisions at $\sqrt{s_{\mathrm{NN}}}$=2.76 TeV with the ATLAS detector at the LHC

The ATLAS Collaboration

Abstract

The variation of the dijet asymmetry with the angle between the leading jet and the second order event-plane in Pb+Pb collisions at $\sqrt{s_{\mathrm{NN}}}$=2.76 TeV is investigated using the ATLAS detector at the LHC. This measurement is extended by constraining the shape of the collision geometry by selecting events based on the magnitude of the second-order flow harmonic. These measurements study the path-length dependence of the dijet asymmetry by requiring the jet pair to traverse different lengths of the medium. A weak dependence of the asymmetry on the angle between the leading jet and the second order event-plane is observed. The asymmetry is systematically larger out-of-plane, where jets traverse on average, a longer path-length in the medium than in-plane, where the path-length is shorter. These results can shed light on the energy-loss mechanism, in which hard-scattered partons lose energy while traversing the hot and dense medium produced in heavy ion collisions.

1. Introduction

Two of the most interesting phenomena observed in relativistic heavy ion collisions are the large anisotropies in the distribution of particles in the plane transverse to the beam axis, and the suppression in the yields of particles having large transverse momentum (p_{T}). The first phenomenon, often termed "flow" [1–4], is generated by collective behavior of the produced medium, which is well described by relativistic hydrodynamics [5, 6]. The second phenomenon, called "jet-quenching", is due to energy loss by the hard-scattered partons produced in the initial stage of the collision as they traverse the medium and are "quenched" [7–11].

The flow measurements are quantified by expanding the azimuthal angle distribution of the produced particles as a Fourier series [12, 13]:

$$\frac{dN}{d\phi} = N_0 \left(1 + \Sigma_{n=1}^{\infty} v_n \cos(n(\phi - \Phi_n))\right), \tag{1}$$

where ϕ is the azimuthal angle of the particle momentum, and v_n and Φ_n are the magnitude and phase of the n^{th} order anisotropy, respectively. The v_n are functions of p_{T}, pseudorapidity (η), particle species and the collision centrality. They are called flow harmonics and the Φ_n are called event-plane (EP) angles. These harmonics are directly related to the spatial asymmetry of the collision geometry, which is quantified by the moments of eccentricity ϵ_n[14, 15]:

$$\epsilon_n = \frac{\sqrt{\langle r^n \cos(n\phi)\rangle^2 + \langle r^n \sin(n\phi)\rangle^2}}{r^n}, \tag{2}$$

$$n\Phi_n^* = \tan^{-1}(\langle r^n \sin(n\phi)\rangle, \langle r^n \cos(n\phi)\rangle) + \pi, \tag{3}$$

where r and ϕ indicate the position of the participating nucleons with respect to the center of mass of the participants and the angular brackets denote averaging over all participants. The Φ_n^* represent the minor axes of the ϵ_n, the directions of the strongest pressure gradients. Thus, the final particle yields, which are driven by the pressure gradients, are expected to be larger along these directions. For the lower order harmonics (n=2,3), the v_n are expected to be proportional to the ϵ_n [16, 17]:

$$\begin{aligned} v_2 e^{i2\Phi_2} &\propto \epsilon_2 e^{i2\Phi_2^*}, \\ v_3 e^{i3\Phi_3} &\propto \epsilon_3 e^{i3\Phi_3^*}. \end{aligned} \tag{4}$$

Thus, the v_2 and v_3 in an event are a direct measure of the shape of the collision geometry for that event.

The jet-quenching measurements are typically studied as the ratio of high-p_{T} particle yields with respect to the binary-collision scaled pp baseline (R_{AA}) [10, 11, 18]. The ATLAS collaboration has introduced an alternative jet-quenching observable called the dijet asymmetry [8], defined as :

$$A_{\mathrm{J}} = \frac{E_{\mathrm{T}}^{\text{lead}} - E_{\mathrm{T}}^{\text{sublead}}}{E_{\mathrm{T}}^{\text{lead}} + E_{\mathrm{T}}^{\text{sublead}}}, \tag{5}$$

where $E_{\mathrm{T}}^{\text{lead}}$ is the transverse energy of the leading (highest E_{T}) jet in the event and $E_{\mathrm{T}}^{\text{sublead}}$ is the transverse energy of the highest E_{T} jet in the opposite hemisphere, defined as $|\Delta\phi| > \pi/2$, where $\Delta\phi$ is the azimuthal angle difference between the jets. The A_{J} is a measure of the E_{T} imbalance between the two highest E_{T} jets in an event. ATLAS measurements have shown a significant enhancement of the asymmetry in central lead-lead collisions as compared to that in peripheral collisions [8, 19].

While flow and jet-quenching have been studied extensively, there have been few studies of the interplay between these "soft" and "hard" aspects of heavy-ion collisions. One such study is the measurement of the jet-v_2 by ATLAS [20], where the dependence of the jet yields was studied with respect to the second-order event-plane angle. A significant v_2^{jet} of 2-5% was observed even at very large jet p_{T}. This v_2^{jet} is a measure of the differential energy loss suffered by hard partons as they traverse different path-lengths of the medium in events characterized by the same collision centrality.

Motivated by the v_2^{jet} measurements, a similar analysis is performed in this note for the dijet asymmetry. The asymmetry is studied for different angles that the leading-jet makes with respect to the second-order EP-angle. The strength of this dependence is quantified by fitting the EP-angle dependence of the event-averaged dijet-asymmetry, $\langle A_{\text{J}} \rangle$, to a second-order harmonic of the form:

$$\langle A_{\text{J}} \rangle = A_J^0 \left(1 + 2c_2 \cos(2(\phi^{\text{lead}} - \Phi_2))\right), \tag{6}$$

where ϕ^{lead} is the azimuthal angle of the leading jet in the dijet pair and Φ_2 is the second-order event-plane angle. The coefficient of the second-order harmonic, c_2, quantifies the EP-angle dependence of the dijet asymmetry. The c_2 measurement is further extended by studying the dependence of A_{J} within the same centrality class, but varying ϵ_2 of the collision geometry. This is done by measuring the A_{J} in events within the same centrality class but with different values of the soft-particle v_2. From Eq. 4 it is seen that binning on the soft-particle v_2 corresponds to selecting on the ϵ_2 of the event. Such event-shape selection has been used extensively in a prior ATLAS publication [21].

The large variation observed in the A_{J} distributions from central to mid-central collisions [8, 19] indicates considerable dependence of the A_{J} on the system size. Glauber-model calculations show that, even in central heavy ion collisions, the ϵ_2 can be quite large [14]. This implies a considerable change in the system size from the in-plane to the out-of-plane directions. The difference between the in-plane and out-of-plane dimensions can be even larger in mid-central collisions, which can have larger eccentricities than central collisions. This would suggest that there would be some variation of the A_{J} distributions when the leading jet is in-plane as compared to when it is out-of-plane.

2. ATLAS detector and trigger

The measurements presented here were performed with the ATLAS calorimeter, inner detector, trigger, and data acquisition systems[1] [22]. The calorimeter system consists of a liquid argon (LAr) electromagnetic (EM) calorimeter ($|\eta|$ <3.2), a steel/scintillator sampling hadronic calorimeter ($|\eta|$<1.7), a LAr hadronic calorimeter (1.5<$|\eta|$<3.2), and a forward calorimeter (FCal) (3.2<$|\eta|$<4.9). Charged-particle tracks were measured over the range $|\eta|$<2.5 using the inner detector [23], which is composed of silicon pixel detectors in the innermost layers, followed by silicon microstrip detectors and a straw-tube transition-radiation tracker ($|\eta|$<2.0), all immersed in a 2T axial magnetic field. The zero-degree calorimeters (ZDCs) are located symmetrically at z=±140 m and cover $|\eta|$>8.3. A ZDC coincidence trigger was defined by requiring a signal consistent with one or more neutrons in each of the calorimeters.

[1] ATLAS uses a right-handed coordinate system with its origin at the nominal interaction point (IP) in the center of the detector and the z-axis along the beam pipe. The x-axis points from the IP to the center of the LHC ring, and the y-axis points upward. Cylindrical coordinates (r, ϕ) are used in the transverse plane, ϕ being the azimuthal angle around the beam pipe. The pseudorapidity is defined in terms of the polar angle θ as $\eta = -\ln\tan(\theta/2)$.

Pb+Pb collisions corresponding to a total integrated luminosity of 0.14 nb^{-1} were analyzed. The events were recorded using either a minimum-bias trigger, formed from the logical OR of triggers based on a ZDC coincidence or the total transverse energy in the event, or a jet trigger implemented using the Pb+Pb jet reconstruction algorithm [10]. The events selected by the jet trigger have at least one jet with transverse energy E_{T}>20 GeV. Event selection and background rejection criteria were applied as described in [2], yielding 53 million and 14 million events in the minimum-bias and jet-triggered samples, respectively. The centrality of Pb+Pb collisions was characterized by $\Sigma E_{\mathrm{T}}^{\mathrm{FCal}}$, the total transverse energy measured in the FCal [2]. The results reported here were obtained using the following centrality intervals defined according to successive percentiles of the $\Sigma E_{\mathrm{T}}^{\mathrm{FCal}}$ distribution ordered from the most central (highest $\Sigma E_{\mathrm{T}}^{\mathrm{FCal}}$) to the most peripheral collisions: (0-10)%, (10-20)%, (20-30)%, (30-40)%, (40-60)%, and (60-80)%. The percentiles were defined after correcting the $\Sigma E_{\mathrm{T}}^{\mathrm{FCal}}$distribution for an estimated 2% minimum-bias trigger inefficiency.

3. Methodology

3.1. Event-plane and event-geometry determination

The second-order event-plane angle and the ellipticity of the events are determined event-by-event by the "second-order flow vector" or "q_2-vector" calculated from the transverse energy (E_{T}) deposited in the FCal [24, 25]:

$$q_{2,x}^{\mathrm{obs}} = \frac{\Sigma E_{\mathrm{T},i}\cos(2\phi_i) - \langle \Sigma E_{\mathrm{T},i}\cos(2\phi_i)\rangle_{\mathrm{evts}}}{\Sigma E_{\mathrm{T},i}}, \quad (7)$$

$$q_{2,y}^{\mathrm{obs}} = \frac{\Sigma E_{\mathrm{T},i}\sin(2\phi_i) - \langle \Sigma E_{\mathrm{T},i}\sin(2\phi_i)\rangle_{\mathrm{evts}}}{\Sigma E_{\mathrm{T},i}}, \quad (8)$$

$$q_2^{\mathrm{obs}} = \sqrt{(q_{2,x}^{\mathrm{obs}})^2 + (q_{2,y}^{\mathrm{obs}})^2}, \quad (9)$$

where the sum is taken over all the calorimeter towers in the FCal, ϕ_i denotes the azimuthal angle and $E_{\mathrm{T},i}$ is the transverse energy deposited in the i^{th} tower. The event-averaged terms $\langle \Sigma E_{\mathrm{T}}\cos(2\phi_i)\rangle_{\mathrm{evts}}$ and $\langle \Sigma E_{\mathrm{T}}\sin(2\phi_i)\rangle_{\mathrm{evts}}$ are subtracted in order to remove detector effects [26]. The q_2^{obs} is the "observed" E_{T}-weighted v_2 in the event. The "observed" here indicates that since the q_2^{obs} is estimated using only the finite number of particles that are in the FCal acceptance, it will fluctuate around the true q_2 (denoted q_2^{true}).

The event geometry classes for a given centrality interval are made by partitioning the FCal q_2^{obs} distributions into classes containing certain fractions of events. For convenience these are denoted as q_2-bins. Since the q_2^{obs} distributions change with centrality, the partitioning into q_2-bins is done in 1%-wide centrality classes, which are then combined to form the q_2-bins for the wider centrality intervals. This procedure is identical to what was done in a prior ATLAS publication [21]. This analysis uses five q_2-bins, each containing a fraction of 0.2 events. The 0.0-0.2 q_2-bin corresponds to 20% of events with the largest q_2^{obs}, i.e. large event ellipticity, while the 0.8-1.0 q_2-bin contains 20% of events with the smallest q_2^{obs}, i.e. small event ellipticity. In order to gain statistics, some of the results are also presented in 0.5-wide q_2-bins.

From the q_2^{obs}-vectors, the second-order EP angle is determined as:

$$\tan(2\Psi_2) = \frac{q_{2,y}^{\mathrm{obs}}}{q_{2,x}^{\mathrm{obs}}}. \quad (10)$$

The finite-number effect that leads to q_2^{obs} being smeared about q_2^{true}, also causes the measured second-order EP angle (Ψ_2) to differ from the "true" second-order EP angle (denoted Φ_2). This requires that the value of the observed c_2 must be corrected by the so-called EP resolution factor [25]:

$$c_2 = \frac{c_2^{\mathrm{obs}}}{\mathrm{Res}\{2\Psi_2\}}, \quad \mathrm{Res}\{2\Psi_2\} = \langle \cos(2(\Psi_2 - \Phi_2)) \rangle_{\mathrm{evts}}, \tag{11}$$

where c_2^{obs} is the "observed" c_2, calculated from the modulation of the $\langle A_{\mathrm{J}} \rangle$ distribution:

$$\langle A_{\mathrm{J}} \rangle = A_J^0 \left(1 + 2c_2^{\mathrm{obs}} \cos(2(\phi^{\mathrm{lead}} - \Psi_2)) \right), \tag{12}$$

and has to be corrected by the EP resolution, $\mathrm{Res}\{2\Psi_2\}$. The sub-event method [25], which has been used in several prior ATLAS analyses, is used to determine the $\mathrm{Res}\{2\Psi_2\}$ for the FCal [2, 4, 24]. The EP resolution for the FCal varies between 0.5 and 0.9 for the centrality classes used in this analysis [4].

For clarity, in the remainder of this note q_2^{obs} is simply called q_2.

3.2. Jet reconstruction

The procedures for jet reconstruction and subtraction of the underlying event are the same as those used in Ref. [10]. They are briefly summarized here. The anti-k_t algorithm, with radius parameter R=0.2, 0.3 and 0.4, was applied to calorimeter towers with segmentation of 0.1×0.1 in $\Delta\eta \times \Delta\phi$. A two-step iterative procedure was used to obtain an event-by-event estimate of the average η-dependent underlying event (UE) energy density while excluding actual jets from the estimate. The jet kinematics were obtained by subtracting the UE energy from the towers within the jet. This subtraction accounts for elliptic flow by modulating the average background density by the magnitude of the elliptic flow measured by the calorimeter, v_2^{calo}, over the interval $|\eta|<3.2$ and excluding regions containing jets. Following reconstruction, the jet energies were corrected to account for the calorimeter energy response using an η- and E_{T}-dependent multiplicative factor that was derived from the MC simulation [27]. In addition to the calorimeter jets, "track jets" were reconstructed by applying the anti-k_t algorithm with the radius parameter of R=0.4 to charged particles with p_{T}>4 GeV. The p_{T} of the track jets, $p_{\mathrm{T}}^{\mathrm{trkjet}}$, is largely unaffected by the UE due to the $p_{\mathrm{T}} > 4$ GeV requirement. To exclude the contribution to the jet yield from UE fluctuations of soft particles falsely identified as calorimeter jets ("fake jets"), the jets used in this analysis were required to be within ΔR=$\sqrt{(\Delta\eta)^2 + (\Delta\phi)^2} < 0.2$ of a track jet with $p_{\mathrm{T}}^{\mathrm{trkjet}}$> 10 GeV or an EM cluster [28] with p_{T}>9 GeV. [2]

The performance of the jet reconstruction was evaluated using the GEANT4-simulated detector response [29, 30] in a Monte Carlo (MC) sample of pp hard-scattering events at $\sqrt{s_{\mathrm{NN}}}$ = 2.76 TeV. The events were produced with the PYTHIA event generator [31] version 6.423 using the AUET2B tune [32] and overlaid on minimum-bias Pb+Pb collisions recorded by ATLAS. Through this embedding procedure, the MC sample contains an UE contribution that is identical in all respects to the data, including azimuthal modulation of the UE due to collective flow. Jets reconstructed in the MC events, using the same algorithms as applied to data, were compared to generator-level jets reconstructed from final-state hadrons, to obtain the jet energy-scale corrections.

Following Ref. [8], the E_{T} thresholds for the A_{J} measurements in this study are $E_{\mathrm{T}}^{\mathrm{lead}}$>100 GeV and $E_{\mathrm{T}}^{\mathrm{sublead}}$>25 GeV. Both jets are required to have $|\eta|$<2.1. The leading jet in an event (for a particular value

[2] This differs from the requirement used in Ref. [10], where the minimum p_{T} was 7 GeV for both track jets and EM clusters.

of R) is defined as the jet with the largest E_{T}. The sub-leading jet is the jet with the largest E_{T} that is located in the opposite hemisphere from the leading jet ($|\phi^{\mathrm{lead}} - \phi^{\mathrm{sublead}}| > \pi/2$).

3.3. MC correction for c_2

Due to jet-energy resolution effects that smear the reconstructed E_{T} of the leading and sub-leading jets about their true values, the reconstructed A_{J} distributions differ from the true A_{J} distributions. The c_2 values obtained using the reconstructed A_{J} distributions are corrected to account for this effect. The correction factors that relate the reconstructed c_2 (c_2^{reco}) to the true c_2 (c_2^{truth}) are derived using MC simulations of the ATLAS detector. The MC events consist of PYTHIA-generated *pp* events overlayed on to Pb+Pb minimum-bias events (Sec. 3.2). The PYTHIA overlay is done irrespective of the EP angle, and thus has $c_2^{\mathrm{truth}} \approx 0$. In order to implement a non-zero c_2^{truth}, the $A_{\mathrm{J}}^{\mathrm{truth}}$ distributions are modified by implementing weights that are dependent on $2|\phi^{\mathrm{lead}} - \Psi_2|$, which give larger asymmetry when the leading jet is produced out-of-plane than in-plane. For several choices of c_2^{truth}, in the range (-0.06,0.04), the c_2^{reco} are determined. The correlations between the c_2^{truth} and c_2^{reco}, which are well described by linear fits, are used to correct the c_2 measured in the data. The slopes from the fits are used as multiplicative correction factors. The intercepts, which are of the order ~0.001, are used as additional offset corrections. The values of the correction factors depend on the exact shape of the original EP-independent $A_{\mathrm{J}}^{\mathrm{truth}}$ distribution, on which the EP-angle dependence is imposed. The correction factors are obtained by using $A_{\mathrm{J}}^{\mathrm{truth}}$ distributions that match the measured A_{J} distributions. These correction factors are used to obtain the final c_2 values. An alternate set of correction factors is obtained by using the A_{J} distributions intrinsic to the PYTHIA tune as $A_{\mathrm{J}}^{\mathrm{truth}}$. The difference between two sets of correction factors is assigned as the systematic uncertainty on the correction factors and used to estimate the systematic uncertainty on c_2.

The correction factors and associated systematic uncertainties are evaluated for each centrality class and for the three different jet radii. Table 1 lists the mean values of the correction factors (averaged over centrality) for reference. The correction factors show only a weak dependence on centrality for the R=0.2 and 0.3 jets (~5%). The centrality dependence for the R=0.4 jets is relatively stronger (~20%). The centrality dependence of the correction factors is taken into account by applying them bin by bin in centrality.

jet-radius parameter	0.2	0.3	0.4
Multiplicative correction factor	1.36±0.04	1.42±0.05	1.50±0.05
Systematic uncertainty in %	13.3	14.3	16.8

Table 1: The centrality-averaged correction factors, which relate c_2^{reco} to c_2^{truth}, and their systematic uncertainties.

4. Systematic uncertainties

The systematic uncertainties in this analysis can be broadly categorized into two classes: uncertainties on the observed c_2^{obs}, and uncertainties on the corrections, namely the EP-resolution and the MC-derived corrections. One of the sources of uncertainty on the c_2^{obs} arises from systematic variations that are seen when checking the sensitivity of the c_2^{obs} to the tail of the A_{J} distribution. This analysis requires that the sub-leading jet has an E_{T}>25 GeV, which introduces an artificial soft cutoff on the maximum A_{J}. The influence of this cut is tested by restricting the analysis to $A_{\mathrm{J}} < 0.6$ and $A_{\mathrm{J}} < 0.55$ and re-evaluating the c_2^{obs}. A second source of systematic uncertainty arises from the criteria used to remove fake jets. As described in Sec. 3.2, the UE fluctuations mis-reconstructed as jets, are rejected as fake-jets if they are not associated, within $\Delta R=\sqrt{(\Delta\eta)^2 + (\Delta\phi)^2} < 0.2$, with a track jet with $p_{\mathrm{T}}^{\mathrm{trkjet}}$> 10 GeV, or with an EM cluster with p_{T} > 9 GeV. However this requirement can also reject real jets. The difference between the c_2^{obs} obtained with and without applying the fake-jet rejection procedure is taken as a systematic uncertainty.

Table 2 summarizes the systematic uncertainties on c_2. The last three columns list the absolute uncertainties on c_2^{obs}. These uncertainties are conservatively taken to be independent of the centrality and the jet-radius parameter. The uncertainties related to the MC-derived correction factors are relative uncertainties and depend on the actual value of the reconstructed c_2. These are assigned as the difference between c_2 values obtained with the two sets of MC-derived correction factors for each centrality interval and jet-radius parameter (see Sec. 3.3). Apart from these, there is an additional uncertainty on the EP-resolution correction, which is also a fractional uncertainty. It is 4.5% in (0-10)% central collisions, then decreases to 1.1% in the (20-30)% centrality class and rises back to 4.5% in the (60-80)% centrality class [4]. The leading source of systematic uncertainty in this measurement is the absolute errors on c_2^{obs}.

Jet-radius parameter	Uncertainty on the MC correction factors [%]	c_2^{obs} syst Error		
		A_{J}<0.6 (0.55)	Fake rejection	Total
0.2	(15-10)	0.003	0.003	0.0042
0.3	(20-10)	0.003	0.003	0.0042
0.4	(30-10)	0.003	0.003	0.0042

Table 2: Systematic uncertainties on c_2 for R=0.2, 0.3 and 0.4 jets. The second column lists the uncertainties on the MC-derived correction factors expressed in percent, as ranges of the form (X-Y), where X% is the uncertainty in the (0-10)% centrality class and Y% is the uncertainty in the (60-80)% centrality class. The systematic uncertainties on c_2^{obs} are given as absolute errors. The total systematic uncertainty on c_2^{obs} represents the sum of the two uncertainties added in quadrature.

5. Results

Figure 1 shows the A_{J} distributions in three different centrality intervals for R=0.2 jets. Within each panel, the two sets of points correspond to two wide q_2-bins, each containing 50% of events with largest (more elliptic collision geometry) and smallest (less elliptic collision geometry) q_2 values. No clear qualitative difference is seen between the two cases. This dependence on the q_2 selection is further studied by plotting the $\langle A_{\mathrm{J}}\rangle$ for five 0.2-wide q_2-bins as shown in Fig. 2 for the same three centrality intervals,. No clear systematic variation of the $\langle A_{\mathrm{J}}\rangle$ with the q_2-bin is observed. To quantify the q_2 independence, the $\langle A_{\mathrm{J}}\rangle$ values are fitted with constant values and the χ^2 of the fits are extracted. These are listed in Table 3 for all centralities and jet-radius parameters used in this analysis. It is seen that the constant fit describes the data quite well in almost all cases, indicating no systematic dependence of $\langle A_{\mathrm{J}}\rangle$ on q_2.

The dependence of the A_{J} on the angle between the leading jet and the second order EP-angle is also studied. Events are selected with the leading jet emitted in one of two different angular intervals with respect to the Ψ_2 plane. The A_{J} distributions for these events are shown in Fig. 3 for R=0.2 jets. No clear difference is visible between the shapes of the distributions measured for events with the leading jet produced in-plane ($2|\phi^{\mathrm{lead}} - \Psi_2|<\pi/4$) and when the leading jet is out-of-plane ($2|\phi^{\mathrm{lead}} - \Psi_2|>3\pi/4$). In order to quantify the change in the asymmetry, the $\langle A_{\mathrm{J}}\rangle$ is evaluated as a function of $2|\phi^{\mathrm{lead}} - \Psi_2|$. This is shown in the bottom panels of Fig. 3 together with fits to a c_2-modulated signal of the form given in Eq. 12. The c_2^{obs} extracted from the fits is small (<0.02). However, it is consistently negative, i.e. the asymmetry is

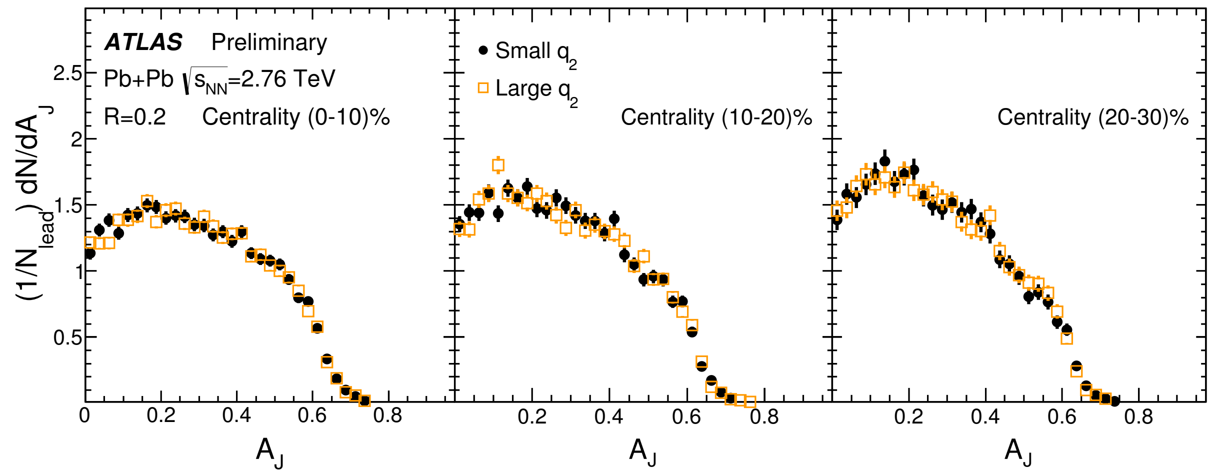

Figure 1: The A_J distributions for R=0.2 jets. Each panel represents a different centrality interval and shows the A_J distributions for 50% of events with largest q_2 (squares) and 50% of events with smallest q_2 (circles). The error-bars represent statistical uncertainties only.

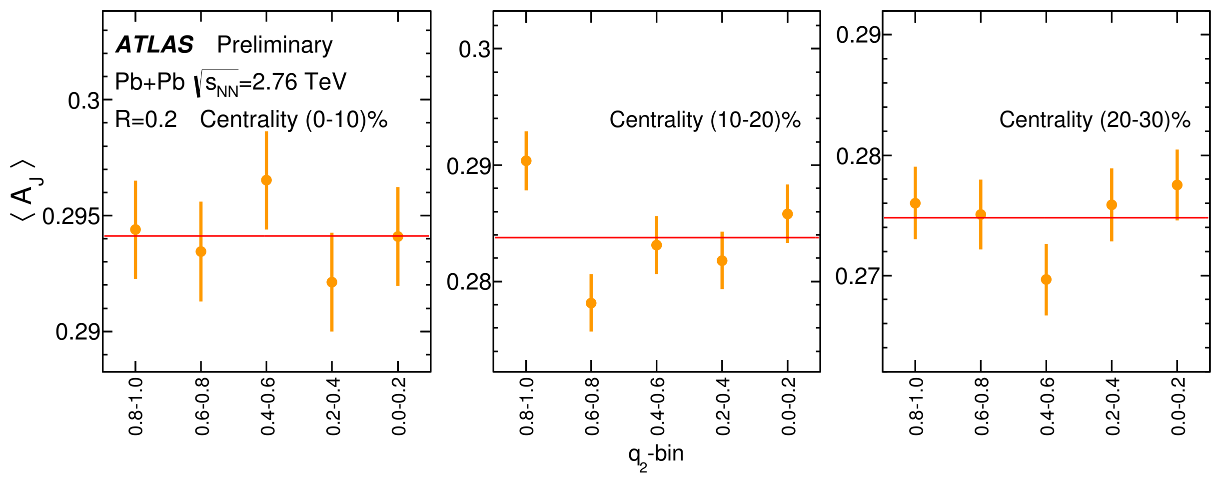

Figure 2: The A_J plotted as a function of q_2-bin (with q_2 increasing from left to right) for R=0.2 jets and for three centrality intervals. The error-bars represent statistical uncertainties only. Horizontal lines denote fits to a constant.

Centrality	χ^2/ndf		
	R=0.2	R=0.3	R=0.4
(0-10)%	0.57	0.27	0.46
(10-20)%	3.34	1.09	1.05
(20-30)%	1.04	0.52	0.74
(30-40)%	0.14	0.12	0.33
(40-60)%	0.92	0.63	0.36
(60-80)%	0.88	1.44	1.27

Table 3: The χ^2/ndf for constant fits to the $\langle A_J \rangle$ vs q_2-bin for R=0.2, 0.3 and 0.4 jets for six different centrality intervals.

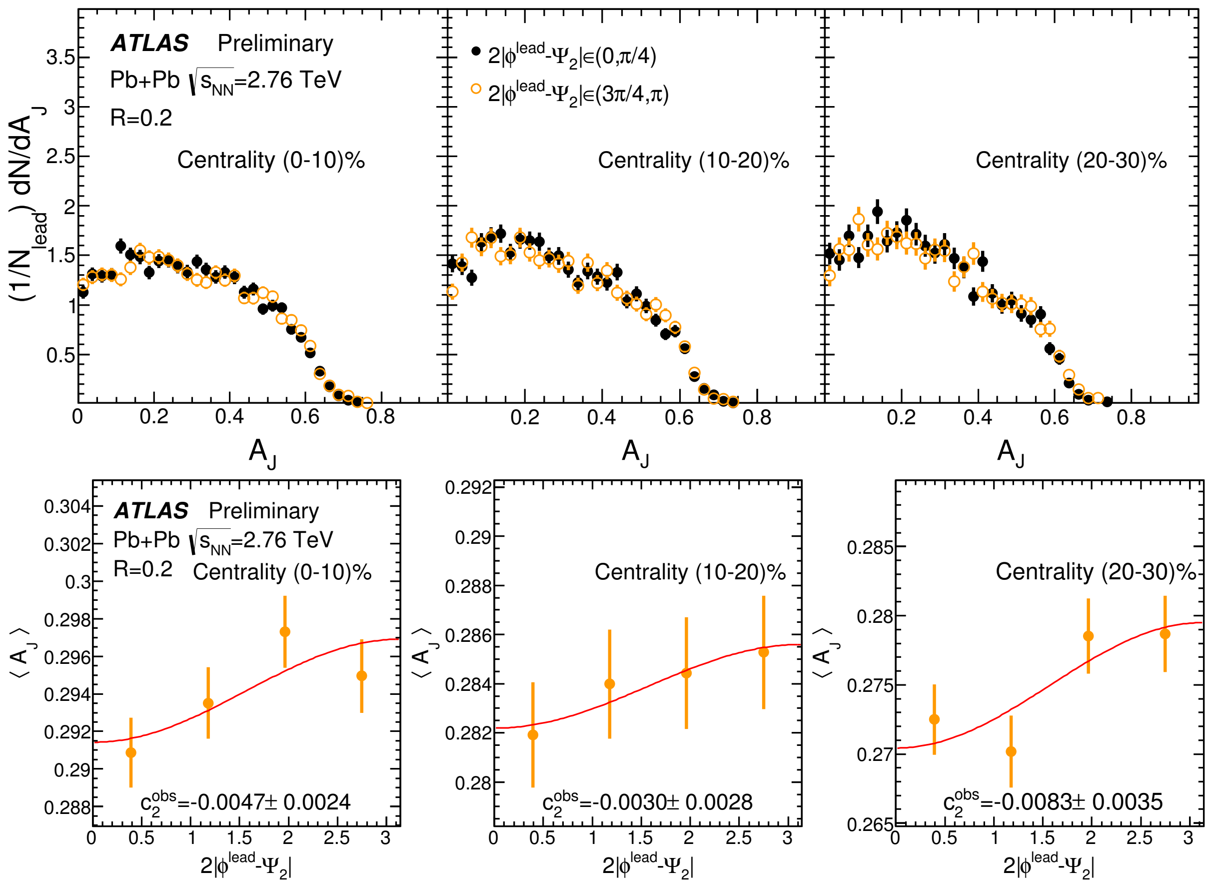

Figure 3: (top) The A_J distributions for R=0.2 jets in three centrality intervals. In each plot, the distributions for two windows in $2|\phi^{lead} - \Psi_2|$ are shown. The error-bars represent statistical uncertainties only. (bottom) The $\langle A_J \rangle$ as a function of $2|\phi^{lead} - \Psi_2|$ together with fits to the second order harmonic term (see Eq. 12). The error-bars represent statistical uncertainties only. The fitted c_2^{obs} parameters are also indicated.

larger, though only slightly, when the leading jet is out-of-plane than when the jet is in-plane. This can be attributed to the longer, on average, path length out-of-plane than in-plane, leading to larger asymmetries in the out-of-plane direction. Figure 4 shows the c_2^{obs} as a function of centrality for the three different jet radii. Negative c_2^{obs} values are systematically seen for R=0.3 and 0.4 jets as well. The absolute magnitude of the c_2^{obs} increases from central to mid-central events and then decreases for the (60-80)% centrality interval.

Since the q_2 is strongly correlated with the ellipticity of the collision geometry, it is expected that A_J should have stronger dependence on the $|\phi^{lead} - \Psi_2|$ for events with larger q_2. In each centrality interval the dependence of $\langle A_J \rangle$ on the EP-angle is evaluated for 50% of events with largest q_2. The resulting c_2^{obs} for R=0.2, 0.3 and 0.4 jets are shown in Fig. 5 as a function of the collision centrality. For comparison, the results for the 50% of events with the smallest q_2 as well as for events without any selection on q_2 (inclusive q_2) are also shown. For all jet-radius parameters, a clear increase of $|c_2^{obs}|$ for events with large q_2 is seen only in the (20-30)% and (30-40)% centrality intervals. In the other centrality intervals, the statistical errors are too large to make any definite conclusions.

Figure 6 shows the final c_2 values after correcting for the EP-resolution as well as for the MC correction

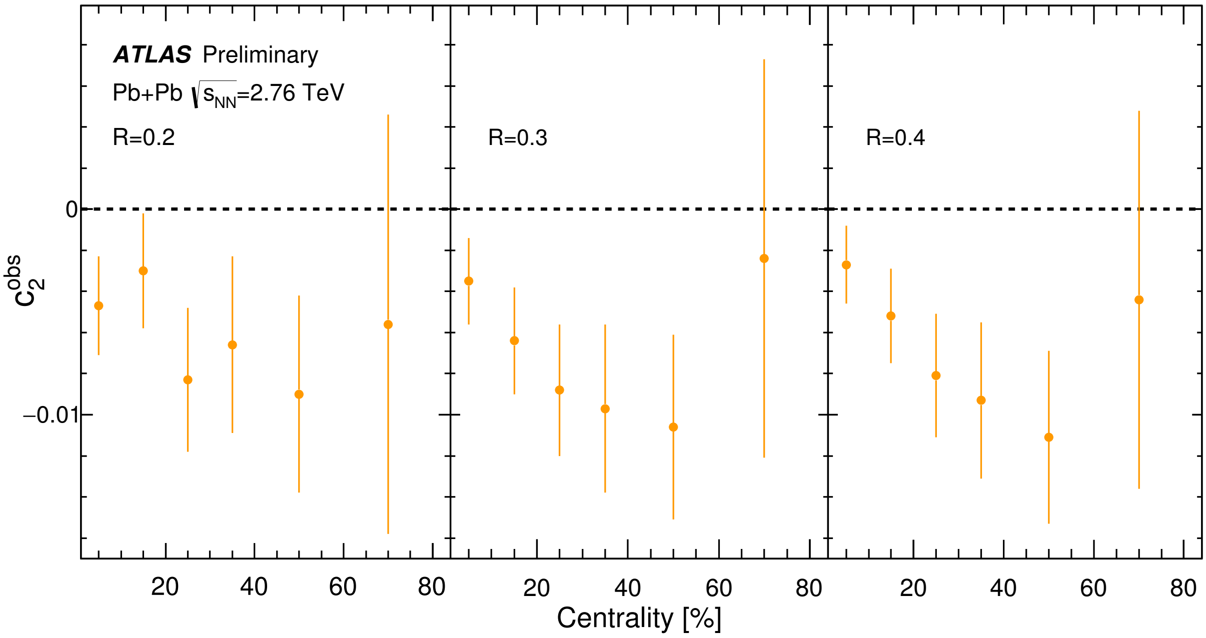

Figure 4: The c_2^{obs} for R=0.2, 0.3 and 0.4 jets as a function of the collision centrality (where the centrality decreases from left to right). The errors are fit errors accounting only for statistical uncertainties.

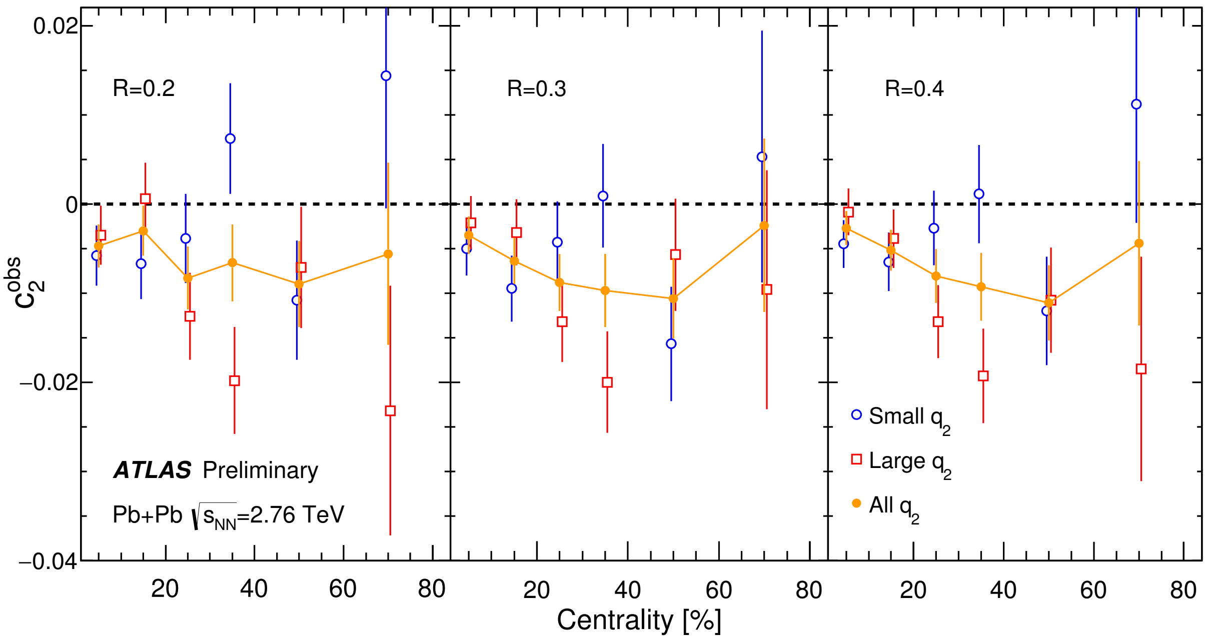

Figure 5: The c_2^{obs} for R=0.2, 0.3 and 0.4 jets as a function of centrality with additional selections on the event-shape (q_2): inclusive events (filled circles), 50% of events with lowest q_2 (open circles) and 50% of events with largest q_2 (squares). The errors are fit errors accounting only for statistical uncertainties.

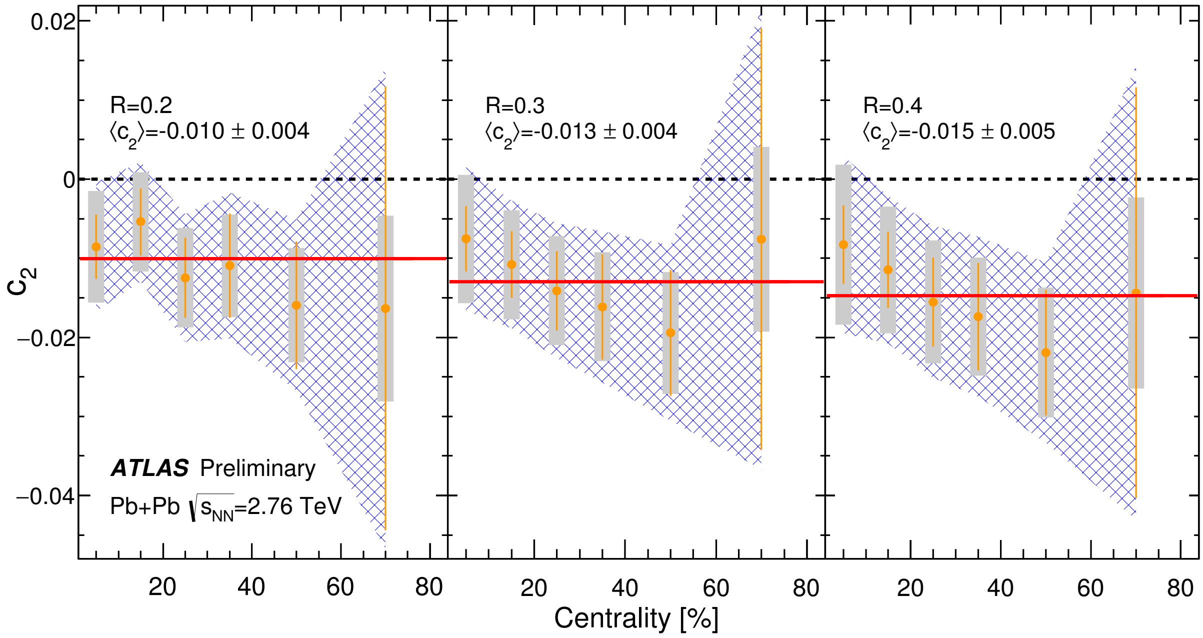

Figure 6: The c_2 corrected for the EP-resolution and MC-derived correction factors as a function of centrality. The vertical grey bands indicate systematic uncertainties and the vertical bars indicate statistical errors. The shaded bands indicate the statistical and systematic uncertainties added in quadrature. The three panels correspond to three jet-radius parameters, as indicated in the plots. Lines show fits to the constant function. The fitted $\langle c_2 \rangle$, averaged over centrality, is also given.

factors. It is seen that the corrected c_2 increases in absolute magnitude from central to mid-central events. The maximum $|c_2|$ is observed in the (40-60)% centrality interval and is of the order of 0.02. The horizontal line is a fit to a constant function to determine the mean value of the c_2 averaged over centrality. The mean value and its error obtained from the fits is given on the plots. It is seen that the centrality averaged c_2 signal is significantly negative.

6. Summary

In this analysis, the dependence of the dijet asymmetry on the angle between the leading jet and the second-order EP-angle is studied. The measurements are performed for anti-k_t jets of R=0.2, 0.3 and 0.4. The dependence of the $\langle A_\mathrm{J} \rangle$ on the EP-angle is quantified by calculating the second Fourier coefficient of the $\langle A_\mathrm{J} \rangle$ azimuthal distribution, termed c_2. The magnitude of the measured c_2 signal is quite small ($\leq 2\%$). However, it is consistently negative, indicating a slightly larger asymmetry when the dijet pair is oriented out-of-plane than in-plane. Within a given centrality interval, events with large q_2, i.e. events with a more elliptic geometry, show an increase in the c_2^{obs} for the (20-30)% and (30-40)% centrality intervals. In other centrality intervals, the statistical precision of the results, obtained with additional selection on q_2, is insufficient to conclude the observation of systematic dependence of $\langle A_J \rangle$ on the EP-angle. The weak c_2 signal in the dijet asymmetry, reported here, together with the significant single jet v_2 [20], and the study of correlated jet production [33] can provide strong constraints on the energy loss mechanism of hard-scattered partons traversing the medium produced in heavy ion collisions.

References

[1] ALICE collaboration, K. Aamodt et. al., *Harmonic decomposition of two-particle angular correlations in Pb-Pb collisions at* $\sqrt{s_{NN}} = 2.76$ *TeV*, Phys. Lett. **B708** (2012) 249–264, arXiv: 1109.2501 [nucl-ex].

[2] ATLAS Collaboration, *Measurement of the pseudorapidity and transverse momentum dependence of the elliptic flow of charged particles in lead-lead collisions at* $\sqrt{s_{\rm NN}} = 2.76$ *TeV with the ATLAS detector*, Phys. Lett. **B707** (2012) 330–348, arXiv: 1108.6018 [hep-ex].

[3] CMS Collaboration, *Centrality dependence of dihadron correlations and azimuthal anisotropy harmonics in PbPb collisions at* $\sqrt{s_{NN}} = 2.76$ *TeV*, Eur. Phys. J. **C72** (2012) 2012, arXiv: 1201.3158 [nucl-ex].

[4] ATLAS Collaboration, *Measurement of the azimuthal anisotropy for charged particle production in* $\sqrt{s_{NN}} = 2.76$ *TeV lead-lead collisions with the ATLAS detector*, Phys. Rev. **C86** (2012) 014907, arXiv: 1203.3087 [hep-ex].

[5] D. A. Teaney, *Viscous Hydrodynamics and the Quark Gluon Plasma* (2009), arXiv: 0905.2433 [nucl-th].

[6] U. Heinz and R. Snellings, *Collective flow and viscosity in relativistic heavy-ion collisions*, Ann. Rev. Nucl. Part. Sci. **63** (2013) 123–151, arXiv: 1301.2826 [nucl-th].

[7] J. Adams et al., *Evidence from* $d + Au$ *measurements for final state suppression of high p(T) hadrons in Au+Au collisions at RHIC*, Phys. Rev. Lett. **91** (2003) 072304, arXiv: nucl-ex/0306024 [nucl-ex].

[8] ATLAS Collaboration, *Observation of a Centrality-Dependent Dijet Asymmetry in Lead-Lead Collisions at* $\sqrt{s_{\rm NN}} = 2.77$ *TeV with the ATLAS Detector at the LHC*, Phys. Rev. Lett. **105** (2010) 252303, arXiv: 1011.6182 [hep-ex].

[9] CMS Collaboration, *Observation and studies of jet quenching in PbPb collisions at nucleon-nucleon center-of-mass energy = 2.76 TeV*, Phys. Rev. **C84** (2011) 024906, arXiv: 1102.1957 [nucl-ex].

[10] ATLAS Collaboration, *Measurement of the jet radius and transverse momentum dependence of inclusive jet suppression in lead-lead collisions at* $\sqrt{s_{\rm NN}}$*= 2.76 TeV with the ATLAS detector*, Phys. Lett. **B719** (2013) 220–241, arXiv: 1208.1967 [hep-ex].

[11] CMS Collaboration, *Study of high-pT charged particle suppression in PbPb compared to pp collisions at* $\sqrt{s_{NN}} = 2.76$ *TeV*, Eur. Phys. J. **C72** (2012) 1945, arXiv: 1202.2554 [nucl-ex].

[12] S. Voloshin and Y. Zhang, *Flow study in relativistic nuclear collisions by Fourier expansion of Azimuthal particle distributions*, Z. Phys. **C70** (1996) 665–672, arXiv: hep-ph/9407282 [hep-ph].

[13] J.-Y. Ollitrault, *Anisotropy as a signature of transverse collective flow*, Phys. Rev. D **46** (1 1992) 229–245.

[14] B. Alver and G. Roland, *Collision geometry fluctuations and triangular flow in heavy-ion collisions*, Phys. Rev. **C81** (2010) 054905, arXiv: 1003.0194 [nucl-th].

[15] D. Teaney and L. Yan, *Triangularity and Dipole Asymmetry in Heavy Ion Collisions*, Phys. Rev. **C83** (2011) 064904, arXiv: 1010.1876 [nucl-th].

[16] F. G. Gardim et al., *Mapping the hydrodynamic response to the initial geometry in heavy-ion collisions*, Phys. Rev. **C85** (2012) 024908, arXiv: 1111.6538 [nucl-th].

[17] Z. Qiu and U. W. Heinz, *Event-by-event shape and flow fluctuations of relativistic heavy-ion collision fireballs*, Phys. Rev. **C84** (2011) 024911, arXiv: 1104.0650 [nucl-th].

[18] ATLAS Collaboration, *Measurements of the Nuclear Modification Factor for Jets in Pb+Pb Collisions at* $\sqrt{s_{\mathrm{NN}}} = 2.76$ *TeV with the ATLAS Detector*, Phys. Rev. Lett. **114**.7 (2015) 072302, arXiv: 1411.2357 [hep-ex].

[19] ATLAS Collaboration, *Centrality dependence of Jet Yields and Jet Fragmentation in Lead-Lead Collisions at* $\sqrt{s_{\mathrm{NN}}} = 2.76$ *TeV with the ATLAS detector at the LHC*, ATLAS-CONF-2011-075 (2011), URL: https://cds.cern.ch/record/1353220.

[20] ATLAS Collaboration, *Measurement of the Azimuthal Angle Dependence of Inclusive Jet Yields in Pb+Pb Collisions at* $\sqrt{s_{NN}} = 2.76$ *TeV with the ATLAS detector*, Phys. Rev. Lett. **111**.15 (2013) 152301, arXiv: 1306.6469 [hep-ex].

[21] ATLAS Collaboration, *Measurement of the correlation between flow harmonics of different order in lead-lead collisions at* $\sqrt{s_{NN}}$*=2.76 TeV with the ATLAS detector* (2015), arXiv: 1504.01289 [hep-ex].

[22] ATLAS Collaboration, *The ATLAS Experiment at the CERN Large Hadron Collider*, JINST **3** (2008) S08003.

[23] ATLAS Collaboration, *The ATLAS Inner Detector commissioning and calibration*, Eur. Phys. J. **C70** (2010) 787–821, arXiv: 1004.5293.

[24] ATLAS Collaboration, *Measurement of event-plane correlations in* $\sqrt{s_{NN}} = 2.76$ *TeV lead-lead collisions with the ATLAS detector*, Phys. Rev. **C90**.2 (2014) 024905, arXiv: 1403.0489 [hep-ex].

[25] A. M. Poskanzer and S. Voloshin, *Methods for analyzing anisotropic flow in relativistic nuclear collisions*, Phys. Rev. **C58** (1998) 1671–1678, arXiv: nucl-ex/9805001 [nucl-ex].

[26] S. Afanasiev et al., *Systematic Studies of Elliptic Flow Measurements in Au+Au Collisions at* $\sqrt{s_{\mathrm{NN}}} = 200$*-GeV*, Phys. Rev. **C80** (2009) 024909, arXiv: 0905.1070 [nucl-ex].

[27] ATLAS Collaboration, *Jet energy measurement with the ATLAS detector in proton-proton collisions at* $\sqrt{s} = 7$ *TeV*, Eur. Phys. J. **C73** (2013) 2304, arXiv: 1112.6426.

[28] ATLAS Collaboration, *Expected Performance of the ATLAS Experiment - Detector, Trigger and Physics* (2009), arXiv: 0901.0512 [hep-ex].

[29] S. Agostinelli et al., *GEANT4: A simulation toolkit*, Nucl. Instrum. Meth. **A506** (2003) 250–303.

[30] ATLAS Collaboration, *The ATLAS Simulation Infrastructure*, Eur. Phys. J. **C70** (2010) 823–874, arXiv: 1005.4568.

[31] T. Sjostrand, S. Mrenna and P. Z. Skands, *PYTHIA 6.4 Physics and Manual*, JHEP **05** (2006) 026, arXiv: hep-ph/0603175.

[32] ATLAS Collaboration, *ATLAS tunes of PYTHIA 6 and Pythia 8 for MC11*, ATL-PHYS-PUB-2011-009 (2011), URL: http://cds.cern.ch/record/1363300.

[33] ATLAS Collaboration, *Measurement of the production of neighbouring jets in lead-lead collisions at $\sqrt{s_{NN}}$ = 2.76 TeV with the ATLAS detector*, ATLAS-CONF-2014-028 (2014), URL: https://cds.cern.ch/record/1703260.

[34] M. L. Miller et al., *Glauber modeling in high energy nuclear collisions*, Ann. Rev. Nucl. Part. Sci. **57** (2007) 205–243, arXiv: nucl-ex/0701025 [nucl-ex].

Auxiliary material

A. In-plane and out-of-plane system size

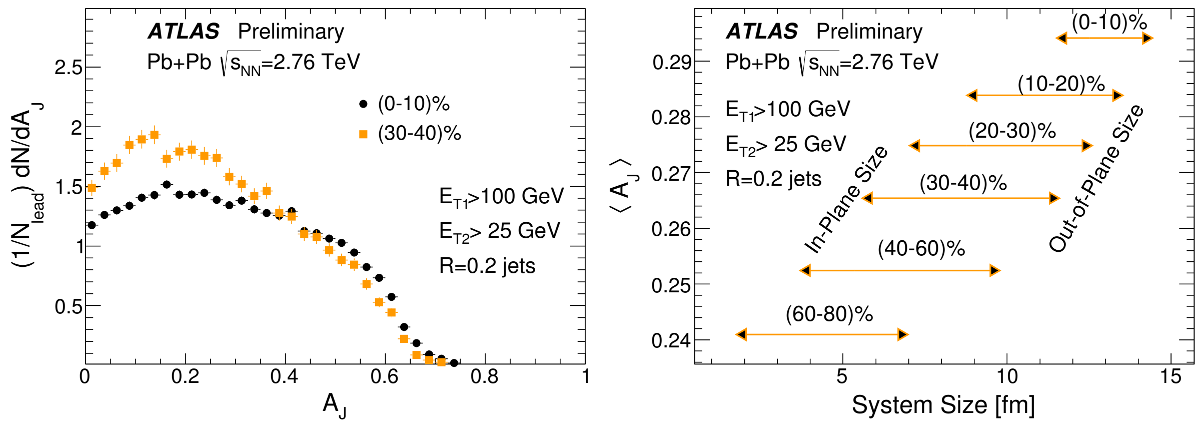

Figure 7: Left Panel: The A_J distributions for two different centrality intervals showing the clear change in the distributions with changing system size. Right Panel: The $\langle A_J \rangle$ for the different centrality intervals. The x-axis range of the arrows indicate the mean system size along the in-plane (at the lower end) and out-of-plane (higher end) directions for the different centrality intervals. These are calculated in a simple geometric picture, in which the colliding nucleons are treated as disks in the transverse plane. The mean in-plane and out-of plane sizes are obtained as $2R_{Pb} - \langle b_{imp} \rangle$ and $\sqrt{4R_{Pb}^2 - \langle b_{imp} \rangle^2}$ respectively, where R_{Pb} is the radius of the Pb nucleus (7.4 fm) and $\langle b_{imp} \rangle$ is the mean impact parameter for the given centrality interval. .

The mean impact parameters $\langle b_{imp} \rangle$ for different centralities calculated in the MC Glauber-model [34] are given in Table 4. In a crude geometric picture, where the colliding nucleons are treated as disks in the transverse plane, the mean in-plane and out-of plane sizes can be obtained as $2R - b_{imp}$ and $\sqrt{4R^2 - (b_{imp})^2}$ respectively, where R is the radius of the Pb nucleus (7.4 fm). Table 4 also lists the mean in-plane and out-of plane system sizes calculated using the above formulae.

Centrality	(0-10)%	(10-20)%	(20-30)%	(30-40)%	(40-60)%	(60-80)%
$\langle b_{imp} \rangle$ [fm]	3.29	6.02	7.77	9.21	11.02	13.05
$\langle$In − plane size$\rangle$ [fm]	11.51	8.78	7.03	5.59	3.78	1.75
$\langle$Out − of − plane size$\rangle$ [fm]	14.43	13.52	12.59	11.59	9.78	6.98

Table 4: The mean impact-parameter ($\langle b_{imp} \rangle$), in-plane and out-of-plane system sizes for various centrality classes calculated in the MC Glauber model.

B. Auxiliary Plots

B.1. Event-shape selection

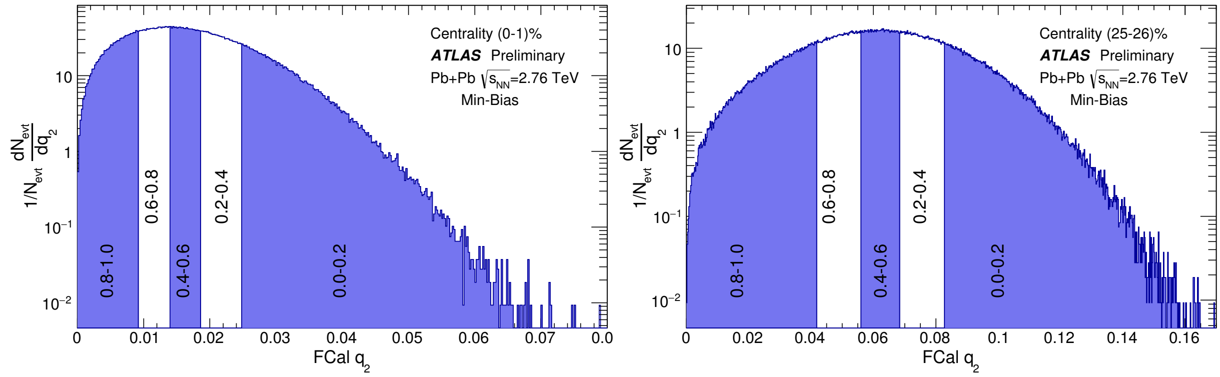

Figure 8: The distributions of magnitude of flow vector q_2 calculated in the FCal via Eq. 9 in two narrow centrality ranges: 0-1% (left) and 25-26% (right). Only minimum-bias events are used to make these plots. The vertical lines indicate the boundary of the q_2 ranges each containing 20% of events.

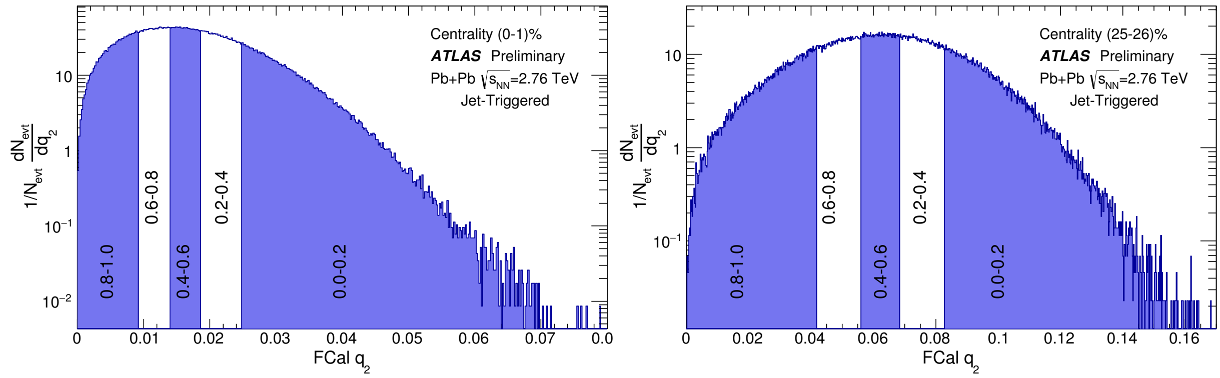

Figure 9: The distributions of magnitude of flow vector q_2 calculated in the FCal via Eq. 9 in two narrow centrality ranges: 0-1% (left) and 25-26% (right). The plots are made for the jet-triggered events, however the bin-edges are determined from the min-bias events of Fig. 8. The vertical lines indicate the boundary of the q_2 ranges each containing 20% of events.

B.2. q_2 dependence

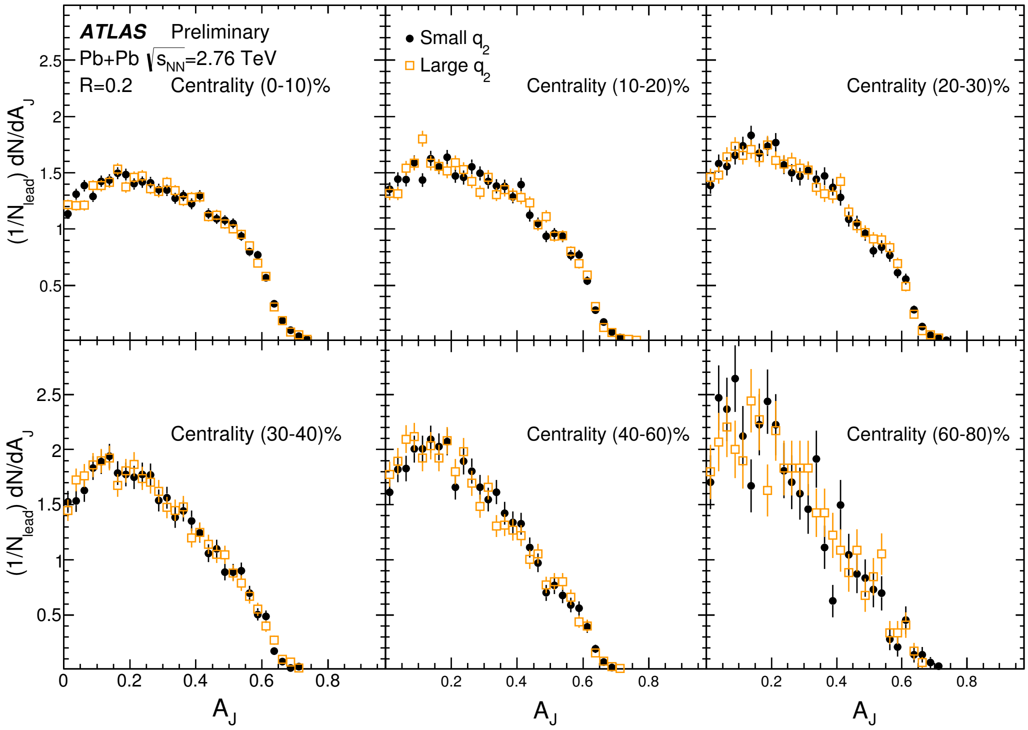

Figure 10: The A_J distributions for R=0.2 jets. Each panel represents a different centrality interval and shows the A_J distributions for 50% of events with largest q_2 (squares) and 50% of events with smallest q_2 (circles). The error-bars represent statistical uncertainties only.

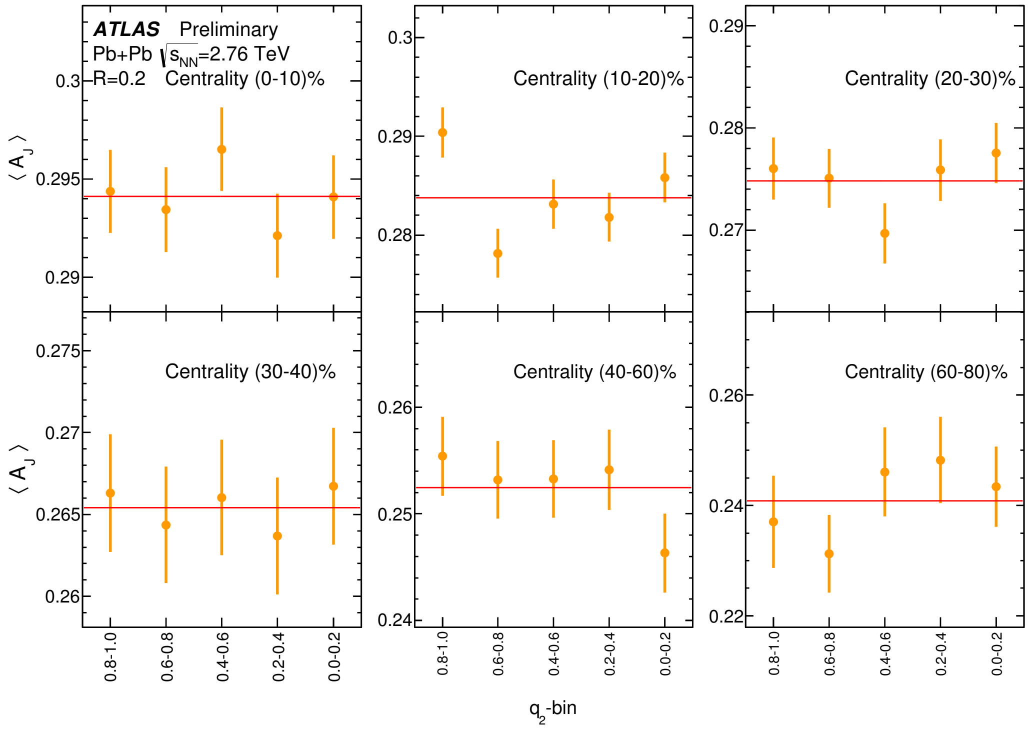

Figure 11: The A_J plotted as a function of q_2-bin (with q_2 increasing from left to right) for R=0.2 jets and for six centrality intervals. Horizontal lines denote fits to a constant. The error-bars represent statistical uncertainties only.

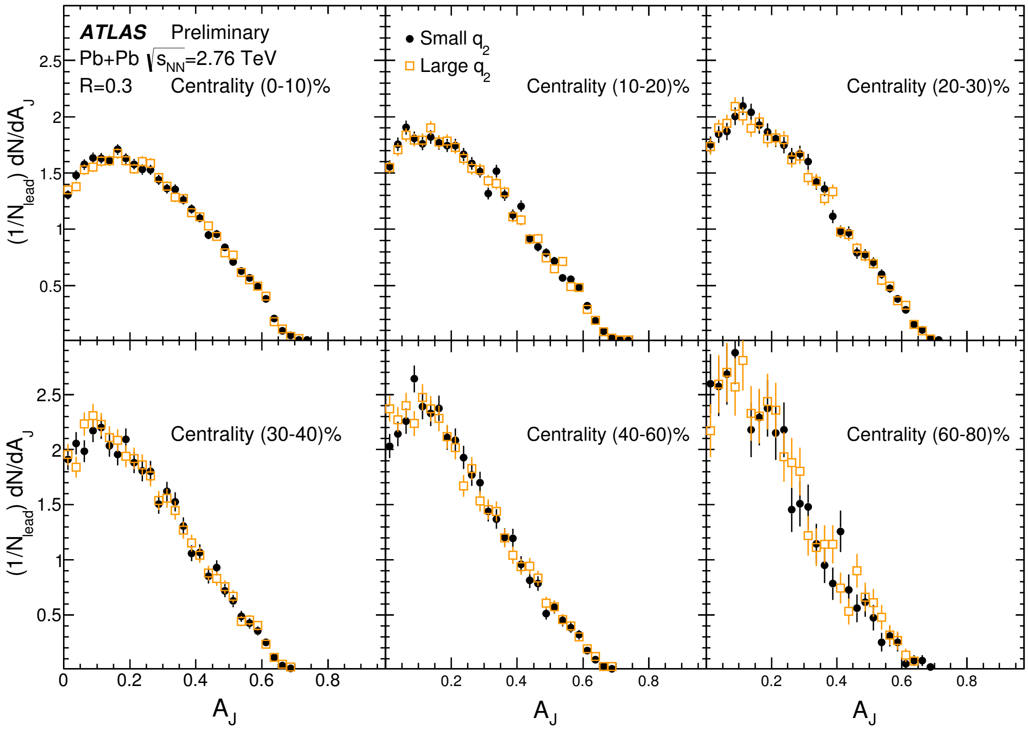

Figure 12: The A_J distributions for R=0.3 jets. Each panel represents a different centrality interval and shows the A_J distributions for 50% of events with largest q_2 (squares) and 50% of events with smallest q_2 (circles). The error-bars represent statistical uncertainties only.

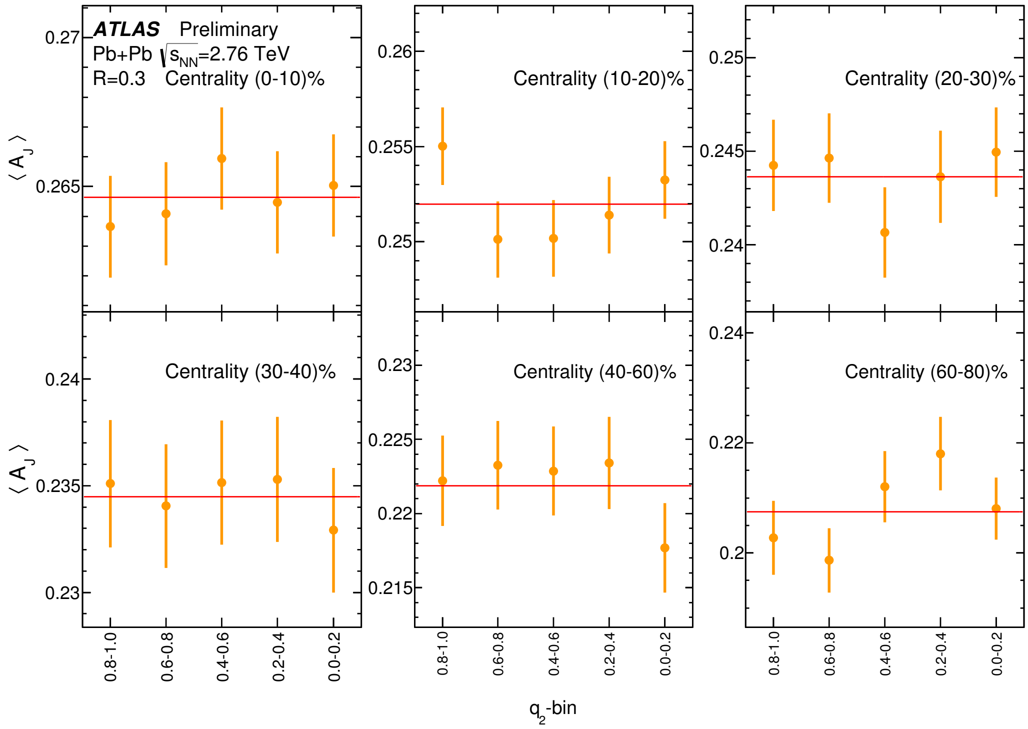

Figure 13: The A_J plotted as a function of q_2-bin (with q_2 increasing from left to right) for R=0.3 jets and for six centrality intervals. Horizontal lines denote fits to a constant. The error-bars represent statistical uncertainties only.

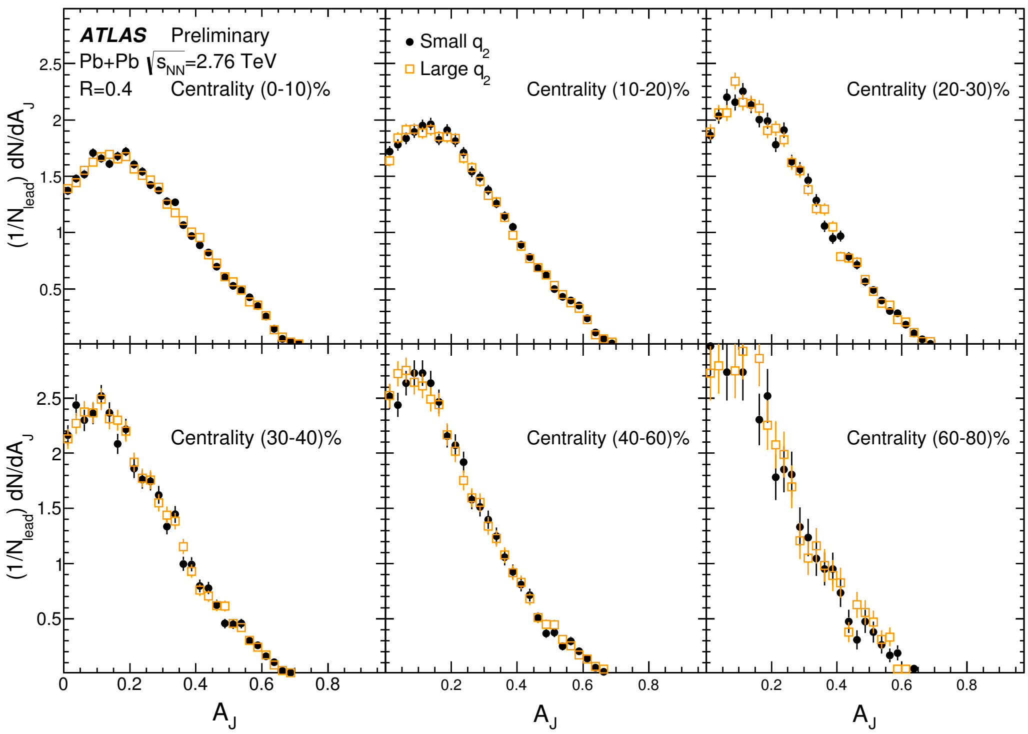

Figure 14: The A_J distributions for R=0.4 jets. Each panel represents a different centrality interval and shows the A_J distributions for 50% of events with largest q_2 (squares) and 50% of events with smallest q_2 (circles). The error-bars represent statistical uncertainties only.

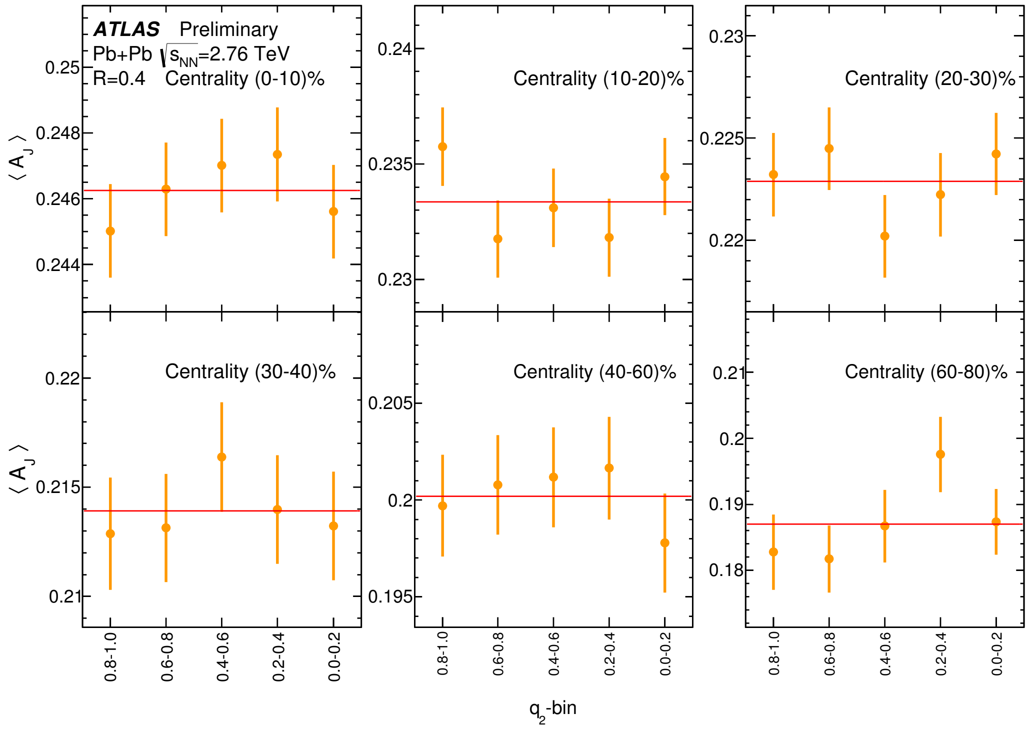

Figure 15: The A_J plotted as a function of q_2-bin (with q_2 increasing from left to right) for R=0.2 jets and for six centrality intervals. Horizontal lines denote fits to a constant. The error-bars represent statistical uncertainties only.

B.3. EP dependence

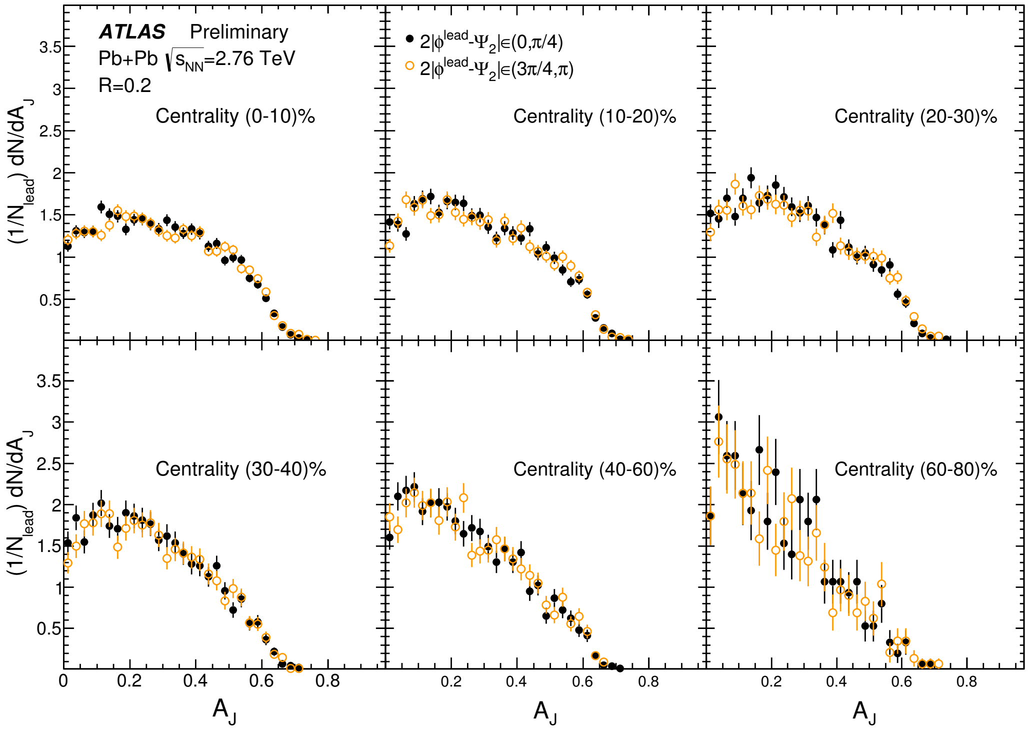

Figure 16: The A_J distributions for R=0.2 jets in six different centrality intervals. In each plot, the distributions for two windows in $2|\phi^{\text{lead}} - \Psi_2|$ are shown. The error-bars represent statistical uncertainties only.

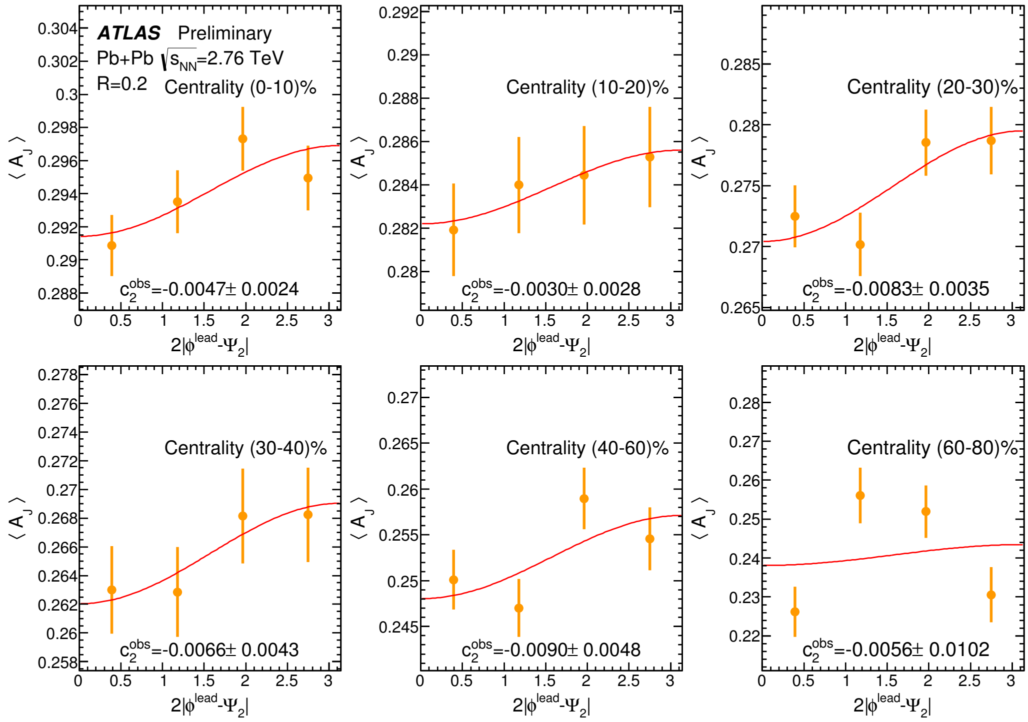

Figure 17: The $\langle A_{\mathrm{J}} \rangle$ as a function of $2|\phi^{\mathrm{lead}} - \Psi_2|$ together with fits to a second order harmonic term for R=0.2 jets. Each panel represents a different centrality interval. The errors are statistical only. The fitted c_2^{obs} parameters are also indicated.

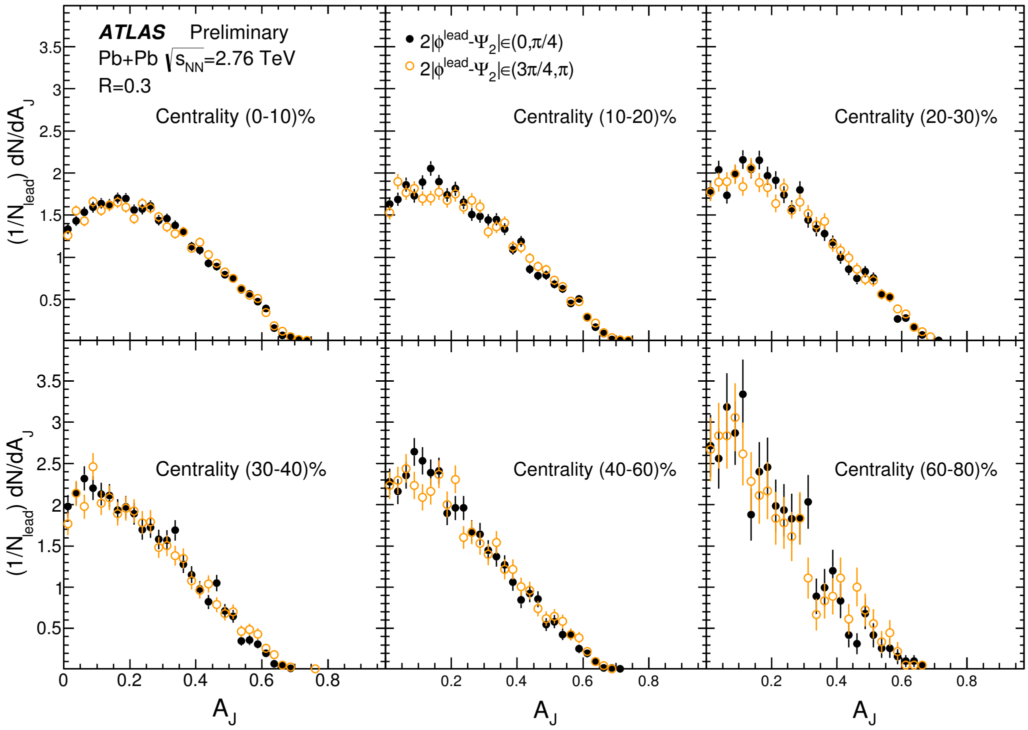

Figure 18: The A_J distributions for R=0.3 jets in six different centrality intervals. In each plot, the distributions for two windows in $2|\phi^{lead} - \Psi_2|$ are shown. The error-bars represent statistical uncertainties only.

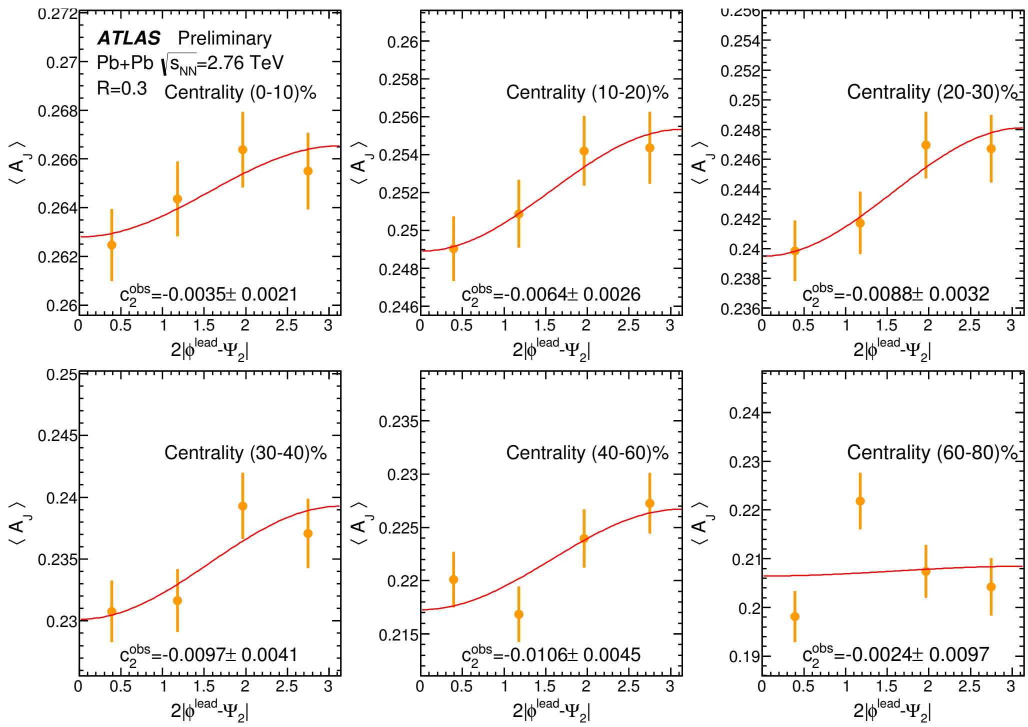

Figure 19: The $\langle A_J \rangle$ as a function of $2|\phi^{lead} - \Psi_2|$ together with fits to a second order harmonic term for R=0.3 jets. Each panel represents a different centrality interval. The errors are statistical only. The fitted c_2^{obs} parameters are also indicated.

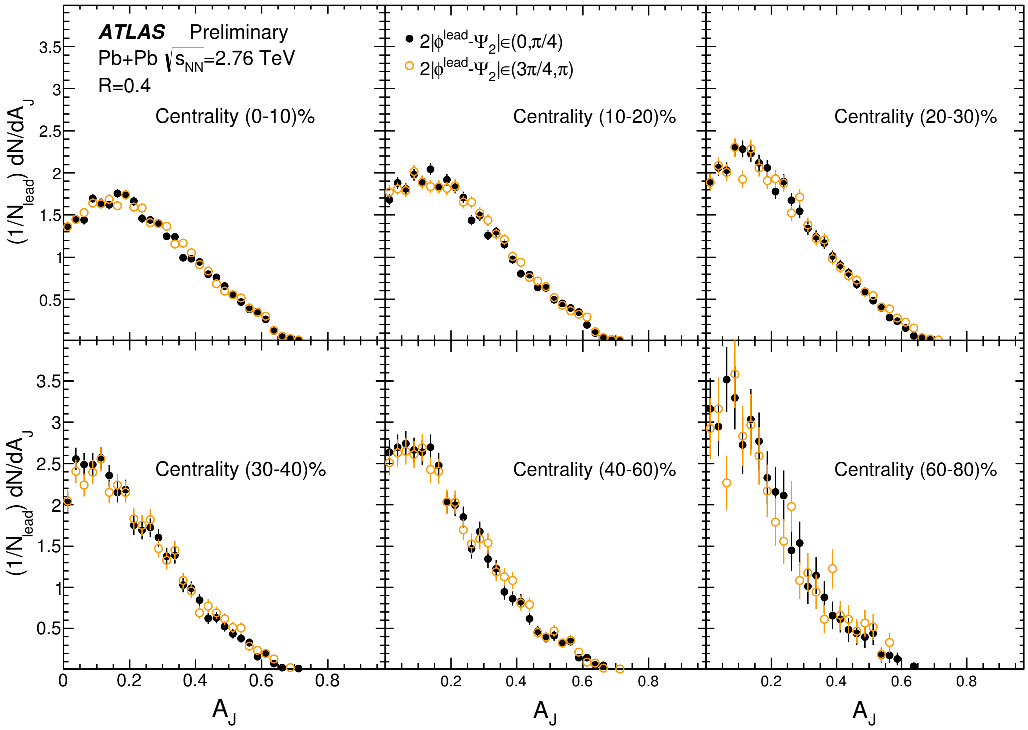

Figure 20: The A_J distributions for R=0.4 jets in six different centrality intervals. In each plot, the distributions for two windows in $2|\phi^\mathrm{lead} - \Psi_2|$ are shown. The error-bars represent statistical uncertainties only.

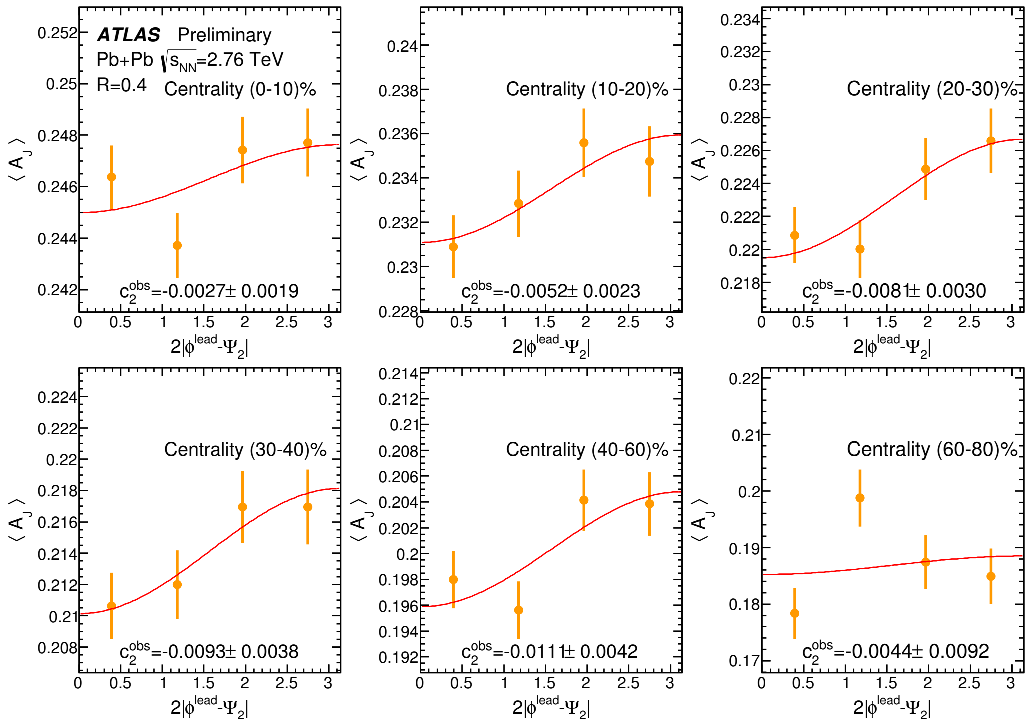

Figure 21: The $\langle A_\mathrm{J} \rangle$ as a function of $2|\phi^\mathrm{lead} - \Psi_2|$ together with fits to a second order harmonic term for R=0.4 jets. Each panel represents a different centrality interval. The errors are statistical only. The fitted c_2^obs parameters are also indicated.